Monthly Notices
of the
ROYAL ASTRONOMICAL SOCIETY

MNRAS **446,** 3975–3991 (2015) doi:10.1093/mnras/stu2392

Hubble Space Telescope scale 3D simulations of MHD disc winds: a rotating two-component jet structure

J. E. Staff,[1,2]★ N. Koning,[3] R. Ouyed,[3] A. Thompson[3] and R. E. Pudritz[4,5]

[1]*Department of Physics and Astronomy, Macquarie University, Sydney, NSW 2109, Australia*
[2]*Department of Physics and Astronomy, Louisiana State University, 202 Nicholson Hall, Tower Dr., Baton Rouge, LA 70803-4001, USA*
[3]*Department of Physics and Astronomy, University of Calgary, 2500 University Drive NW, Calgary, AB T2N 1N4, Canada*
[4]*Department of Physics and Astronomy, McMaster University, Hamilton, ON L8S 4M1, Canada*
[5]*Origins Institute, ABB 241, McMaster University, Hamilton, ON L8S 4M1, Canada*

Accepted 2014 November 11. Received 2014 November 2; in original form 2014 May 28

ABSTRACT

We present the results of large scale, three-dimensional magnetohydrodynamics simulations of disc winds for different initial magnetic field configurations. The jets are followed from the source to 90 au scale, which covers several pixels of *Hubble Space Telescope* images of nearby protostellar jets. Our simulations show that jets are heated along their length by many shocks. We compute the emission lines that are produced, and find excellent agreement with observations. The jet width is found to be between 20 and 30 au while the maximum velocities perpendicular to the jet are found to be up to above 100 km s^{-1}. The initially less open magnetic field configuration simulations result in a wider, two-component jet; a cylindrically shaped outer jet surrounding a narrow and much faster, inner jet. These simulations preserve the underlying Keplerian rotation profile of the inner jet to large distances from the source. However, for the initially most open magnetic field configuration the kink mode creates a narrow corkscrew-like jet without a clear Keplerian rotation profile and even regions where we observe rotation opposite to the disc (counter-rotating). The RW Aur jet is narrow, indicating that the disc field in that case is very open meaning the jet can contain a counter-rotating component that we suggest explains why observations of rotation in this jet have given confusing results. Thus magnetized disc winds from underlying Keplerian discs can develop rotation profiles far down the jet that is not Keplerian.

Key words: MHD – methods: numerical – stars: protostars – ISM: jets and outflows.

1 INTRODUCTION

Astrophysical jets are observed in a range of astrophysical objects including protostars, X-ray binaries, active galactic nuclei (AGN), and more. Common to many of these sites is a central object surrounded by an accretion disc. The magnetocentrifugal mechanism described in Blandford & Payne (1982) explains how jets can be launched, accelerated, and collimated by a large-scale magnetic field threading the disc. While this mechanism was originally developed in the context of AGN jets, its applicability to ubiquitous protostellar jets has been substantially developed for over three decades through detailed theoretical models (e.g. Pelletier & Pudritz 1992; Ferreira 1997; Krasnopolsky & Königl 2002), advanced simulations in two dimensions (e.g. Shibata & Uchida 1985; Uchida & Shibata 1985; Ustyugova et al. 1995; Ouyed, Pudritz & Stone 1997; Kato, Kudoh & Shibata 2002; Ramsey & Clarke 2011) and three dimensions (e.g. Ouyed, Clarke & Pudritz 2003; Anderson et al. 2006; Moll 2009; Staff et al. 2010), and tested against the ever increasing high-resolution observations (e.g. Bacciotti et al. 2000, 2002; Woitas et al. 2005; Ray et al. 2007; Coffey, Bacciotti & Podio 2008; Coffey et al. 2012). The magnetohydrodynamic (MHD) disc wind is now arguably the most extensively tested theory available for protostellar jets and outflows (see reviews by e.g. McKee & Ostriker 2007; Pudritz et al. 2007; Frank et al. 2014).

Jets from young stellar objects have been seen from both low-mass protostars, for instance the RW Aur jet studied in Coffey et al. (2012) and Woitas et al. (2005), and also from massive protostars (e.g. G35.2 observed by Zhang et al. 2013). Cesaroni et al. (2013) noticed similarities between the observed jet from the massive protostar IRAS 20126+4104 and the simulated jets shown in Staff et al. (2010). While it may well be that the magnetocentrifugal mechanism can explain jets from both low-mass and massive protostars, as well as other jets like those in AGN (see e.g. Staff et al. 2013), in this paper we focus our attention on jets from low-mass (i.e. solar mass) protostars.

★ E-mail: jan.staff@mq.edu.au

The magnetocentrifugal mechanism is not the only proposed theoretical model for young stellar object (YSO) jet formation. An alternative model is the X-wind model (e.g. Shu et al. 2000) in which a Keplerian rotation profile of the jet is not expected. The two main goals of the simulations presented here are to look for rotation and magnetic structures in jets that lead to features reminiscent of observed jets, and that can be tracked through observations of emission lines. It may be expected that jets launched by the magnetocentrifugal mechanism may have a Keplerian rotation profile, as it will be launched from an extended region of the disc.

We presented two three-dimensional (3D) MHD simulations of protostellar jets, with two different initial magnetic field configurations [Ouyed–Pudritz (OP) and Blandford–Payne (BP) configurations; see Section 2] in Staff et al. (2010). In that paper, as in this, we focused on magnetic field configurations, whose poloidal magnetic field strength at the disc surface falls off as power laws with disc radius (r_o) as $B_p \propto r_o^{\mu-1}$, where $-0.5 \leq \mu < 0$ defining the degree of inclination and decline of the field along the surface of the disc (Jørgensen, Ouyed & Christensen 2001). The simulation box in both cases was 60 au long and 30 au wide in the two directions perpendicular to the jet. One interesting result was that in the OP simulation (with the less open initial magnetic field configuration), a two-component jet structure developed. That is, a narrow, inner jet surrounded by, but separated from, a cylindrical-shaped outer jet. No such outer jet was found in the BP simulation. However, the outer part of the BP jet was starting to leave the grid, and it was unclear if this was the reason for the lack of an outer jet. This therefore motivated us to increase the size of the simulation box, and repeat the OP and BP simulations. In addition, we also ran two simulations with new initial magnetic field configurations, $\mu = -0.12$ which is an intermediate configuration between the OP ($\mu = -0.01$; Ouyed & Pudritz 1997) and BP ($\mu = -0.25$; Blandford & Payne 1982) configurations (see Section 2 for an explanation of the μ parameter), and Pelletier–Pudritz (PP, $\mu = -0.5$; Pelletier & Pudritz 1992) which is even more open than the BP configuration. This way, a more systematic study of the effect of the initial magnetic field configuration on the resulting jet can be made. In this paper we present the results of these four simulations.

In Staff et al. (2010) we computed synthetic [O I] λ6300 emission lines based on the MHD simulations presented there. Using these emission lines, we found good agreement between the simulations and observations for the jet width, temperature, density, velocity, and the mass flux in the jets. We have again been focusing our effort on computing synthetic emission line maps from our 3D simulations, and use these to interpret the *Hubble Space Telescope* (*HST*) observations of YSO jets. In this work we show that jets may have a Keplerian rotation profile, although not in all cases.

Velocity gradients in jets perpendicular to the jet axis can be interpreted as jet rotation, as Choi, Kang & Tatematsu (2011) did for NGC 1333 and Lee et al. (2008) did for HH 212. RW Aur has also shown a velocity gradient perpendicular to the jet axis (Woitas et al. 2005), however, Cabrit et al. (2006) found that this was opposite to the disc rotation. Coffey et al. (2012) re-investigated the RW Aur jet and found a velocity gradient in a direction opposite of that found by Woitas et al. (2005), but consistent with the disc rotation. However, later observations did not show this gradient any more. While these velocity gradients may be indicative of jet rotation, the findings by Coffey et al. (2012) illustrate that the explanation may not be that simple. In this paper we investigate the rotation in disc winds, and offer explanations for these seemingly contradictory observations.

Using the *HST*, nearby protostellar jets in the Taurus cloud at a distance of 140 pc can be resolved down to 14 au scale. This is very interesting as it allows observations of the region where the jet is generated and collimated (for a summary, see Ray et al. 2007). Also of importance is that in recent years, increased computer power has allowed 3D MHD simulations of protostellar jets to be extended to large scales while still being able to resolve and simulate the source. Anderson et al. (2006) used a simulation box extending out to 12 au, while Moll (2009) used a simulation box extending out to 60 au, a similar length to what we used in Staff et al. (2010). As can be inferred, these latter simulations can cover several pixels of jets observed by the *HST*, and that is important as it allows for direct comparison between the properties of observed jets and simulated jets. In this work we have extended the simulation box from Staff et al. (2010) to 90 au.

This paper is organized as follows. We start by briefly describing our numerical set-up in Section 2. In Section 3 we present the tools and the strategy we use to compute emission lines, position–velocity (PV) diagrams, and the visualization of our simulations. Results are presented in Section 4 with a summary and a conclusion given in Section 5.

2 NUMERICAL APPROACH

We use the ZEUSMP code (Norman 2000) to simulate a protostellar jet being launched from a Keplerian accretion disc. The simulation set-up discussed here is based on Staff et al. (2010), however, the simulation box has been extended to $3000r_i$ in the jet direction (from $2000r_i$ in the previous paper), and to $\pm 900r_i$ in the two directions perpendicular to the jet axis (from $\pm 500r_i$). For reasons outlined in Ouyed et al. (2003) we use a Cartesian coordinate system (x_1, x_2, x_3). In addition we break the quadrantal symmetry by wobbling the disc, as described in Ouyed et al. (2003). The grid is 1536 zones in the x_1 direction (i.e. the direction of propagation of the jet), and 500 zones in the x_2 and x_3 directions (the directions parallel to the plane of the disc). This grid is separated into a uniform grid of $200 \times 100 \times 100$ zones located just above the disc and centred around the axis that extends from -25 to $25r_i$ in the x_2 and x_3 directions, and from 0 to 100 in the x_1 direction. The remainder of the large grid (200 zones on either side of the uniform grid in the x_2 and x_3 directions, and 1336 zones in extension to the uniform grid in the x_1 direction) is ratioed, extending the large grid from $-900r_i$ to $900r_i$ in the x_2 and x_3 directions and out to $3000r_i$ in the x_1 direction. Although the boundaries in our simulation are outflow boundaries, it is important that very little mass leaves the grid, as this may lead to incorrect results. We avoid this by using such a large simulation box.

In the simulations presented in this paper, as well as in many previous works, the disc is treated as a boundary condition (e.g. Ouyed & Pudritz 1997; Krasnopolsky, Li & Blandford 1999; Ouyed et al. 2003; Anderson et al. 2006; Staff et al. 2010; Ramsey & Clarke 2011). The protostar in our simulations is located at the $x_1 = 0$ boundary as in Ouyed et al. (2003). More recently, a few attempts have been made to simulate self-consistently both the disc and the jet launching (e.g. Zanni et al. 2007; Murphy, Ferreira & Zanni 2010; Sheikhnezami et al. 2012). The fixed physical conditions in the accretion disc are another key simplification in our model. From experience, properly simulating the disc and reaching scales that we are simulating are beyond the current state-of-the-art simulations. Some attempts have been made by various groups at simulating the disc and the jet in 3D but these simulations do not capture the acceleration, and collimation, and far out regions which is our main goal. In part, this simplification may be justified by the fact that typically accretion discs will evolve on longer time-scales than their associated jets.

The density profile of the hydrostatically stable accretion disc corona is given by $\rho = r^{-3/2}$, for $r < 1000r_i$, where $r = \sqrt{x_1^2 + x_2^2 + x_3^2}$. The density profile of the corona smoothly transits to a uniform density for $r > 1000r_i$. This configuration remains stable and cures numerical issues induced by extremely low density in the coarse grid. This does not affect the outcome of the simulations. The density profile in the disc matches that of the overlaying corona except for much higher density in the disc (i.e. a density jump of a factor of 100 between the disc and the corona) imposed by pressure balance. The corona and the accretion disc (a fixed boundary in our simulations) are threaded by an initially purely poloidal, force free and current free, magnetic field. Most accretion disc models used assume power-law distributions of density and temperature, so it is natural to assume power-law structure for the fields, i.e. $B_p \propto r_o^{\mu-1}$.

The velocity profile in the disc is Keplerian, $v_\phi \propto 1/\sqrt{r}$. At the inner and outer edges of the disc, the velocity profile is smoothed to avoid a cusp as discussed in Ouyed et al. (2003) (see appendix A1 and simulation E in that paper). The outer edge of the disc was set to $r_{out} = 80r_i$. However, the outer edge has less impact on our results since in most of our simulations the jets are launched from close the innermost regions of the disc. So as long as $r_{out} \gg r_i$ increasing r_{out} does not make much of a difference.

For our fiducial values (i.e. setting the mass of the protostar to $1\,M_\odot$), we estimate $r_{in} \simeq 0.03$ au (Ouyed & Pudritz 1997) assuming that the stellar magnetosphere truncates the disc roughly at this radius. For a comparison, recent studies of the inner circumstellar disc of S CrA N (a T Tauri star) with the Very Large Telescope Interferometer (VLTI) suggest that $r_{in} \sim 0.11$ au for a corresponding $\sim 1.5\,M_\odot$ protostar (Vural et al. 2012). Hence, the simulations are run on a grid extending out to 90 au along the jet axis, and 27 au on either side of the jet axis (compared to 15 au on either side of the jet axis and 60 au long in Staff et al. 2010).

2.1 Parameters in the model

As listed in Staff et al. (2010) (see also Ouyed et al. 2003) the parameters of the model can be divided into disc parameters and those defining the corona. The parameters related to the disc are the following. (i) The injection speed v_{inj} which is set to a tiny fraction of the Keplerian speed (v_K) so that $v_{x_1} = v_{inj}v_\phi$ with $v_{inj} = 0.003v_K$ in all of our simulations, which makes it subsonic. The injection speed defines the mass loading. As discussed in Ouyed & Pudritz (1999), v_{inj} has an upper bound set by the fact that we want the sonic point to be resolved in the simulations. Numerically it is hard to lower v_{inj} much, as mass is being depleted from the region just above the disc faster than it is being resupplied from the disc. Such low-density regions can easily cause problems in numerical simulations like these. (ii) Pressure balance between the corona and the underlying disc fixes the density jump between the two. This defines another parameter $\eta_i = 100$ which is the ratio between the disc density and the density in the overlaying corona. The remaining parameters define the corona: (i) the corona is kept in hydrostatic balance by thermal pressure which defines a parameter $\delta = 5/2$; (ii) the ratio of gas pressure to magnetic pressure in the corona at r_i (i.e. at the inner disc boundary) was set to equipartition value, i.e. $\beta = 1$.

The magnetic field configuration (given by μ with $B_p \propto r_o^{\mu-1}$ along the disc's surface) is the one parameter which is varied. In order to investigate the role of the initial magnetic field geometry in launching and collimating jets, we analyse results from four configurations: the OP (with $\mu = -0.01$), the BP (with $\mu = -0.25$), the PP (with $\mu = -0.5$), and a fourth configuration between the OP and BP one with $\mu = -0.12$.

3 VISUALIZATION AND DIAGNOSTIC TOOLS

We visualize the simulations using two softwares namely VISIT (used to generate Figs 1–3 in this paper; see https://wci.llnl.gov/codes/visit/) and SHAPE (Steffen et al. 2011) for the other figures. SHAPE is capable of visualizing HDF data in a variety of forbidden emission lines making it an ideal tool for generating observation comparable images and PV diagrams.

SHAPE implements a ray-casting radiative transfer algorithm to calculate the emission reaching the observer. For each pixel in the final image, a ray is cast from the back of the 3D grid to the front (observer). As the ray passes through the grid, emission coefficients are calculated according to the density, temperature, and species contained within the grid cell. For the current simulations, we assume a two-level system under optically thin conditions in local thermodynamic equilibrium (LTE) and calculate the emission coefficients for [Cl IV] 74 500 Å, [S II] 6730 Å, and Mg II 2796 Å. The line data for these transitions were obtained from the Chianti spectral line data base (Dere et al. 1997). The critical densities for these lines are ~ 1, $\sim 10^4$, and $\sim 10^{15}$ cm^{-3} for the [Cl IV], [S II], and Mg II transitions, respectively. Typical electron densities in our simulations are around 10^4 cm^{-3} (assuming an electron fraction of 0.1). Therefore our three lines represent transitions with critical densities well below, equal to, and well above the jet densities. For densities much less than critical, the emission depends on n^2, and for densities much higher than critical, it depends on n (see e.g. Osterbrock & Ferland 2006). Our chosen lines therefore represent both extreme cases and the transition from one regime to the other.

The dimensionless temperature of the gas used in the calculation of the emission coefficients can be found by using a polytropic equation of state (EOS, $P \propto \rho^\gamma$, $\gamma = 5/3$; see Staff et al. 2010): $T = \rho^{\gamma-1}$. If the Alfvén Mach number (M_A) is greater than 0.3 we assume the gas to be shocked and the temperature is then found by using $T = \rho^{\gamma-1}\frac{M_A^2}{\beta}\frac{\gamma-1}{2}$, where $\beta = P_g/P_B$ is the plasma β (for details, see Ouyed & Pudritz 1993).

With these tools we can present our simulations as seen in [Cl IV], [S II], and Mg II. The [S II] and Mg II lines are known to be strong, leading to higher signal-to-noise ratio when observing real jets (e.g. Bacciotti et al. 2000; Coffey et al. 2012). Finally, SHAPE allows us to easily generate PV diagrams which as we show later turn out to be crucial when comparing the different simulations.

Our use of a polytropic EOS is a limitation. Nevertheless, this ansatz (which effectively bypasses the energy equation) corresponds to situation where the combined effects of cooling and heating simulate a tendency towards a state of local constant entropy. This also tremendously simplifies the numerical set-up. Except in cases where the shocks are dynamically important (Ouyed et al. 2003), this simplification allows us to test the code against analytical solutions (e.g. Blandford & Payne 1982).

We compute the radiation in the post-processing step (using SHAPE), assuming heating from shocks which may appear inconsistent with the previous statement, while at the same time assuming that neither the radiation nor the cooling plays a dynamically important part in the simulations. These are simplifications that are necessary at this point, but should be addressed in future calculations. Likewise, we assume a constant ionization fraction, while in reality it may well vary throughout the jet and also change over time, for instance in shocks.

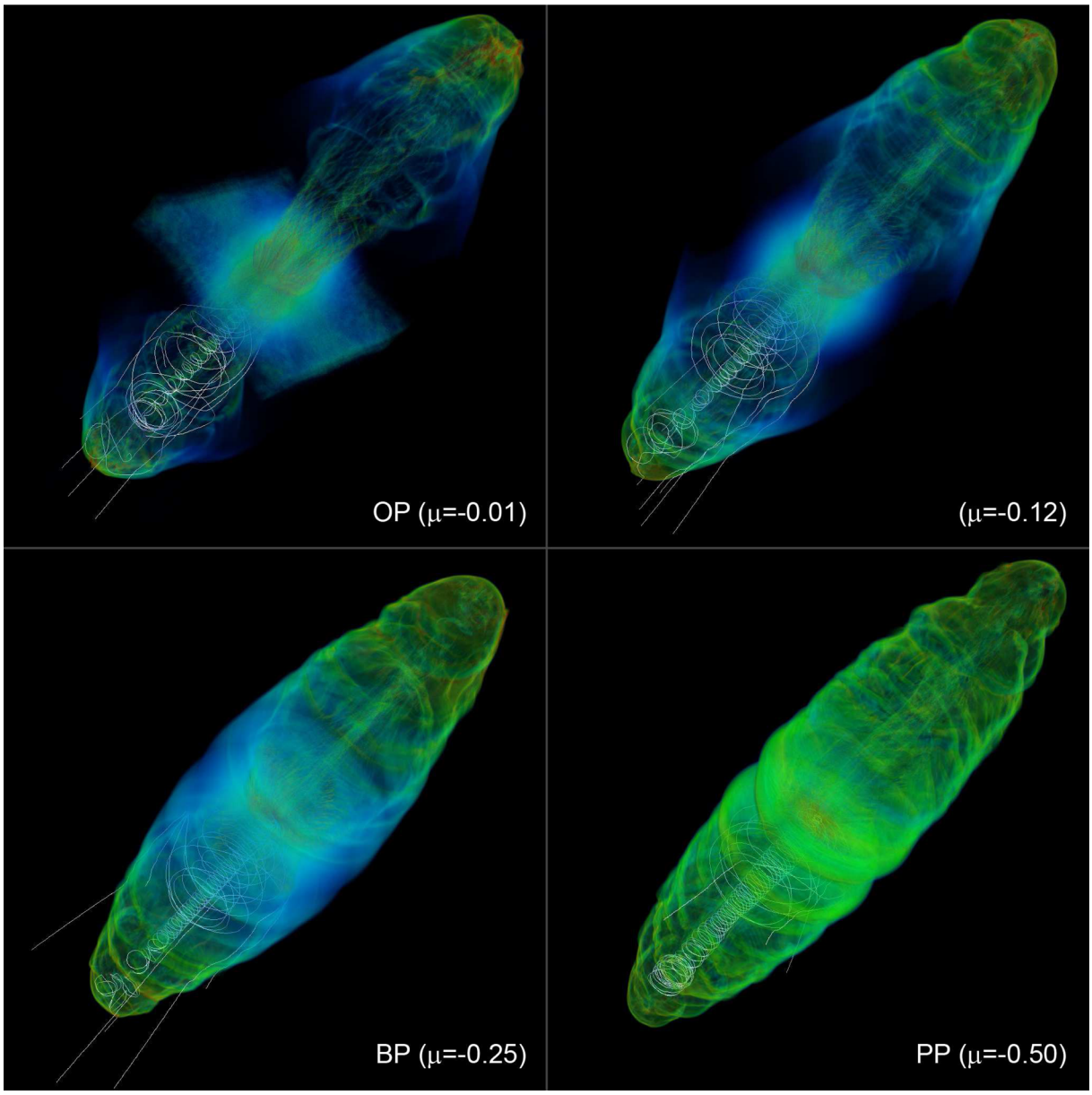

Figure 1. 3D figures of the final jet structure in the four simulations. The jet is only simulated in one hemisphere. To visualize it, it is mirrored in the disc plane to make it appear bipolar. The field lines are only drawn in one hemisphere in each figure, so that the density structure can be best visualized. See http://quarknova.ucalgary.ca/MHD.html for the relevant animations.

4 RESULTS

Fig. 1 shows the final density and magnetic field structure of the jets with different magnetic field structure on the disc (different μ). The protostar and the disc are located in the middle of the figure. For all the different magnetic field configurations on the disc, we find a narrow jet extending out along the axis. Close to the disc and the protostar it is relatively straight, but farther away it starts to twist up in a corkscrew-like fashion (see also Section 4.2). In the front of the jet, a bow shock is clearly visible. More negative μ leads to a higher Mach number, and therefore the bow shock is bent more strongly backwards in those cases. Extending backwards from the bow shock is a cocoon of material that has been processed by the bow shock. In the BP and PP simulation, this cocoon stays on the grid throughout the entire simulation, while in the OP and $\mu = -0.12$ simulations part of this material is pushed off the grid.

Fig. 2 shows the field lines only, and only in one hemisphere, for better clarity. Independently of the magnetic field on the disc, the field lines wrap up tightly around the narrow jet, indicating that the hoop stress is collimating the jet. In the PP jet we even find tighter collimation of the field lines further out in the jet, indicating increased collimation of the jet at larger distances. For all the magnetic field configurations, there is also a 'spine' in the middle of the jet of mostly poloidal field that helps stabilize the jet (for more about jet stability, see Ouyed et al. 2003). This mostly poloidal field originates from the protostar (not the disc), explaining why it is not being wrapped up (the footpoint is not orbiting). The most tightly

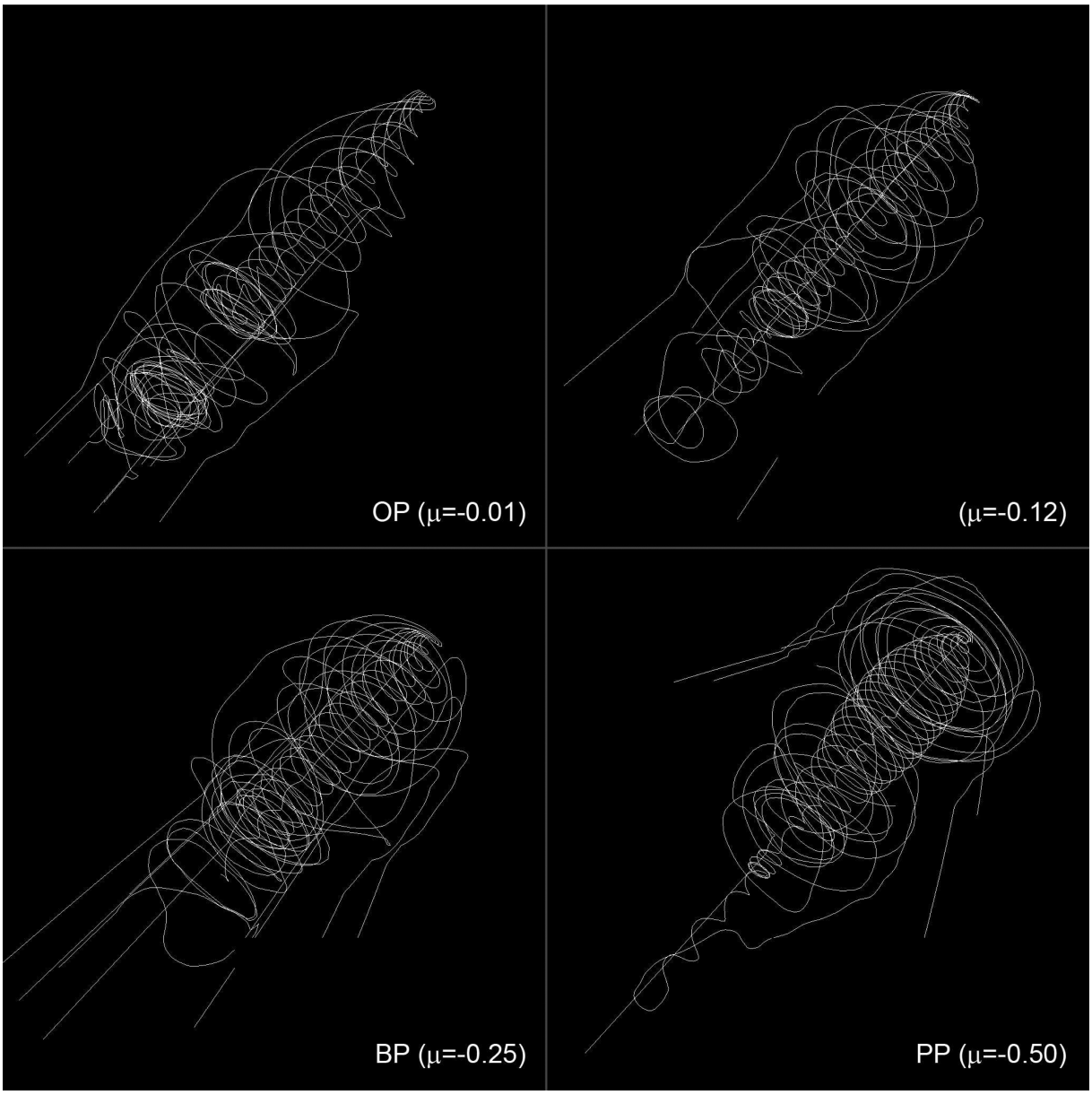

Figure 2. The magnetic field lines for each jet (only one hemisphere is shown). The disc and the protostar are in the upper right-hand corner of each figure. The PP jet shows a very strong collimation halfway through the jet (which is also visible in Fig. 1). The footpoints for the field lines are chosen slightly differently than in Fig. 1, which is why the field lines look slightly different. However, the general features remain in both figures.

wound up field originates in the very inner part of the disc. For all the configurations, some field lines do not wind up but are seen to be mostly straight. These field lines originate just a few au into the disc, illustrating that the jet originates from the very innermost 1 or 2 au of the disc.

4.1 The two-component jet

As was pointed out in Staff et al. (2010), the OP jet is a two-component jet, consisting of a narrow, inner jet, and surrounded by a cylindrical-shaped outer jet. The BP simulation in Staff et al. (2010) did not show any such outer jet, and it was questioned whether this was related to the fact that mass had started flowing off the side of the grid in that simulation. With the bigger grid, we here again find that the OP jet has a two-component structure like found before (collimated by the less tightly twisted field lines anchored farther out in the disc), and we find only one clear component in the BP jet, although there is a very faint outer jet surrounding the inner part (close to the $x_1 = 0$ boundary) of the BP jet. The $\mu = -0.12$ configuration, which is intermediate between OP ($\mu = -0.01$) and BP ($\mu = -0.25$), also results in a clear outer jet component, at least for the first half of the jet. There is no outer jet seen in the PP simulation. This can be seen in the density structure in Fig. 1.

We show a larger version of the OP jet in Fig. 3 to better illustrate the features of that jet. Outside the inner jet, other field lines with footpoints farther out in the disc are seen to wrap up, although less tightly. We find that field lines with footpoint within $\sim 15 r_i$ ($\sim$0.45 au) in the OP jet twist up tightly around the inner jet. Field lines with footpoints outside of this are less tightly wound up and leads to the outer jet. Beyond $\sim 50 r_i$ ($\sim$1.5 au), field lines do not

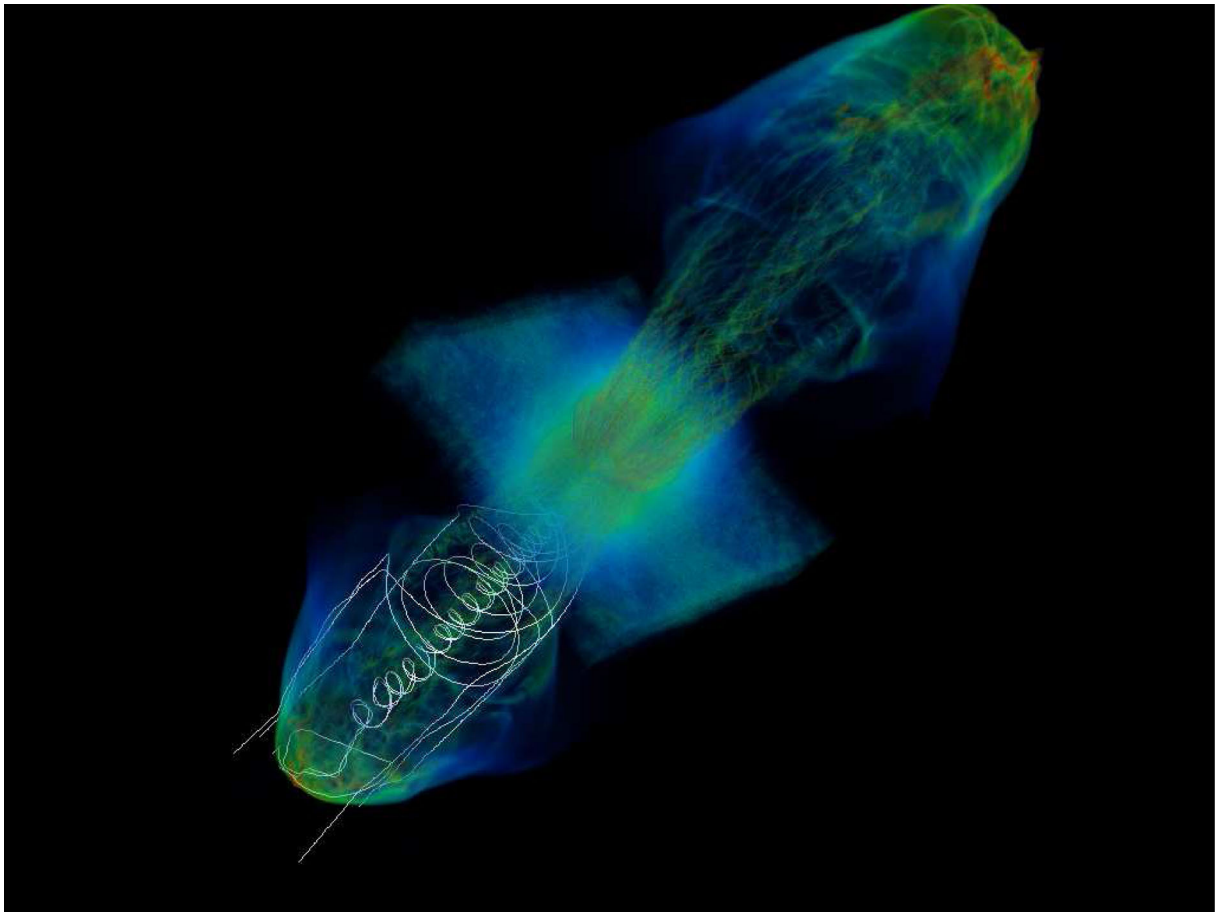

Figure 3. A larger version of the OP jet from Fig. 1 at the end of the simulation, shown for better clarity. The two-component jet structure (i.e. a narrow inner jet surrounded by a cylindrical-shaped outer jet) is clearly visible, as is the twisted magnetic field, especially around the inner jet. The bow shock at the front of the jet is also clearly visible. The protostar and the disc are hidden in the middle. As in Fig. 1 we only draw the magnetic field lines in one hemisphere to better illustrate the details of the density structure.

twist up much but are mostly straight and we do not expect these to contribute much to the jet. In contrast to this, field lines with footpoint inside of $\sim 20 r_{\rm i}$ ($\sim$0.6 au) in the PP simulation twist up tightly around the jet. Footpoints farther out twist up with a much larger radius, but do not propagate much forward along the jet (see Fig. 2) and will therefore not contribute to any jet. This is why there is no outer jet in the PP simulation.

In the $\mu = -0.12$ simulation, the bow shock is also bent more sharply backwards than in the OP simulation, and the outer jet is therefore terminated earlier upon interacting with the cocoon. Thus, it seems that the shape of the bow shock and the resulting backflowing current affect the evolution of the second jet component.

The recollimation effect of the PP jet is also reflected in the toroidal velocity, as shown in Fig. 4. The rotating jet narrows as the twisting field lines also narrow, showing that the jet itself is more collimated farther away from the disc. We show in Fig. 5 the mass density and the momentum density for each simulation in a slice along the jet axis, zoomed in on a region close to the disc. In the OP jet, the momentum–density vectors point mostly forward. For the initially more open magnetic field configurations, the momentum–density vectors point less forward, and more away from the axis. In the PP jet, material is flowing almost perpendicular away from the axis 15–20 au from the axis, close to the disc boundary.

In Figs 6–8 we show the different simulated jets as they appear in [Cl IV] 74500 Å, [S II] 6730 Å, and Mg II 2796 Å, respectively. In Figs 9–11 we present PV diagrams in the same lines taken perpendicular to the jet at 15, 45, and 75 au from the disc. Because of their vastly different critical densities, the jet appears quite different in each line. In the Mg II line image, the core of the jet is much brighter than the surrounding cocoon, and it completely dominates the picture. For the [S II] line, parts of the core of the jet are above the quenching density, while the outer parts are below. As a consequence, the core of the jet is not that bright compared to the surrounding cocoon, and hence this can be seen as well. For the [Cl IV], the quenching density is below the density in most of the jet. We note that the emission in Figs 6–8 is not normalized to the same factor. As a consequence the jet would appear orders of magnitude dimmer in [Cl IV] than in [S II] or Mg II.

The emission from the inner, dense part of the jet is much enhanced in the Mg II line (since this is below the critical density), and the outer jet is not visible at all. The PV diagram found using this line is quite messy reflecting the structure of the high densities in the inner jet. The outer jet shows up very clearly in the [Cl IV] line PV diagram, especially for the OP jet at 45 au, as a strong increase in the velocity around 10 au. The outer jet is also visible in the $\mu = -0.12$ jet at both 15 and 45 au, and also in the BP jet at 15 au. It might be that given enough time an outer jet will set up as the surrounding cocoon drifts outwards, if enough mass can be channelled that way. The outer jet is also visible in the [S II] images. In Staff et al. (2010) we identified the outer jet in the OP

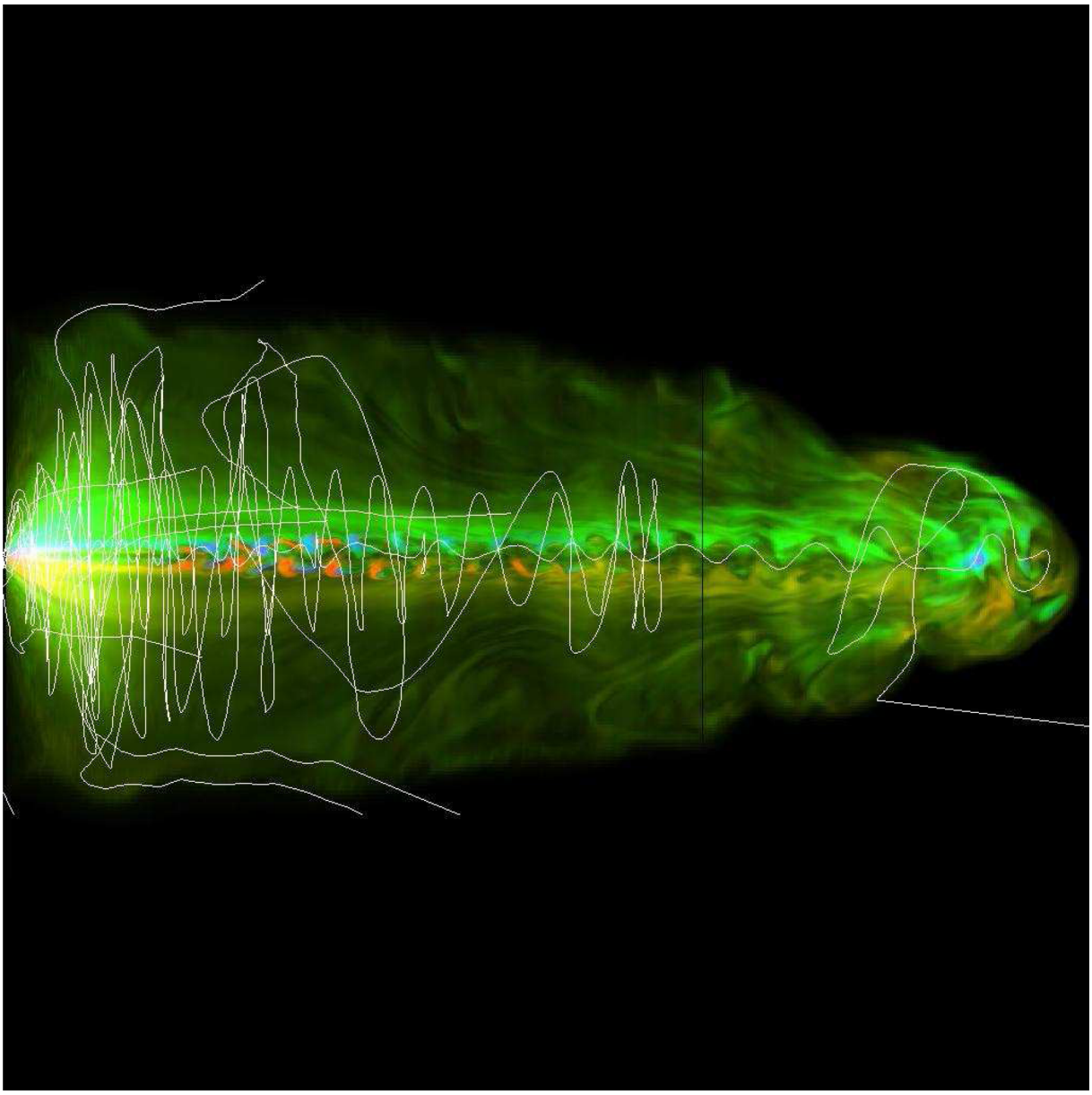

Figure 4. Magnetic field lines and toroidal velocity for the PP jet. The disc and protostar are on the left-hand boundary. The brighter colours illustrate higher intensity radiation. The field lines show an increased collimation about halfway through the jet. At the same place, the high-intensity part of the jet narrows, showing that in the PP jet the collimation increases further out in the jet.

simulation with a strong increase in toroidal velocity. We still see this for the OP and $\mu = -0.12$ jets, but for the BP jet there is only a weak increase in the toroidal velocity. The cocoon does not appear to interfere at this point, and we therefore conclude that no strong outer jet develops in the BP configuration.

The jet width can be read off from the line maps and the PV diagram. We find it by looking at the emission line maps (Figs 6–8). The [S II] line gives the best estimate for the true jet width, as it picks up most of the jet but not the cocoon. The [Cl IV] sees the entire cocoon surrounding the jet. On the scale shown here, the Mg II line does not see either the outer jet or the cocoon for either simulation. We emphasize that this is simply because of how we separate the contours in our plots. Since the high-density inner jet is much brighter than the outer jet, this is where the contours are for the Mg II line. We also emphasize that in the Mg II line, the inner jet is much brighter than any part of the [S II] or [Cl IV] line maps. We note that the simulated jet is still very young, and in real jets this cocoon would likely have been pushed sufficiently far away that it would not confuse the observations.

Ignoring the effects of the cocoon, we find by looking at the line maps of the configurations with the more open disc magnetic field (i.e. the more rapidly declining magnetic field distribution on the disc, or more negative μ) that the jets appear most collimated. This is in part because of the lack of an outer jet. The PP jet opens up close to the disc, but narrows around 35 au (as discussed earlier). A somewhat similar effect can be seen in the BP jet, although it is a much smaller narrowing than in the PP jet. The inner jet in $\mu = -0.12$ and the OP jet does not show such narrowing, rather it appears to continue widening with a somewhat constant opening angle throughout the length of the jet. We find, by looking at the

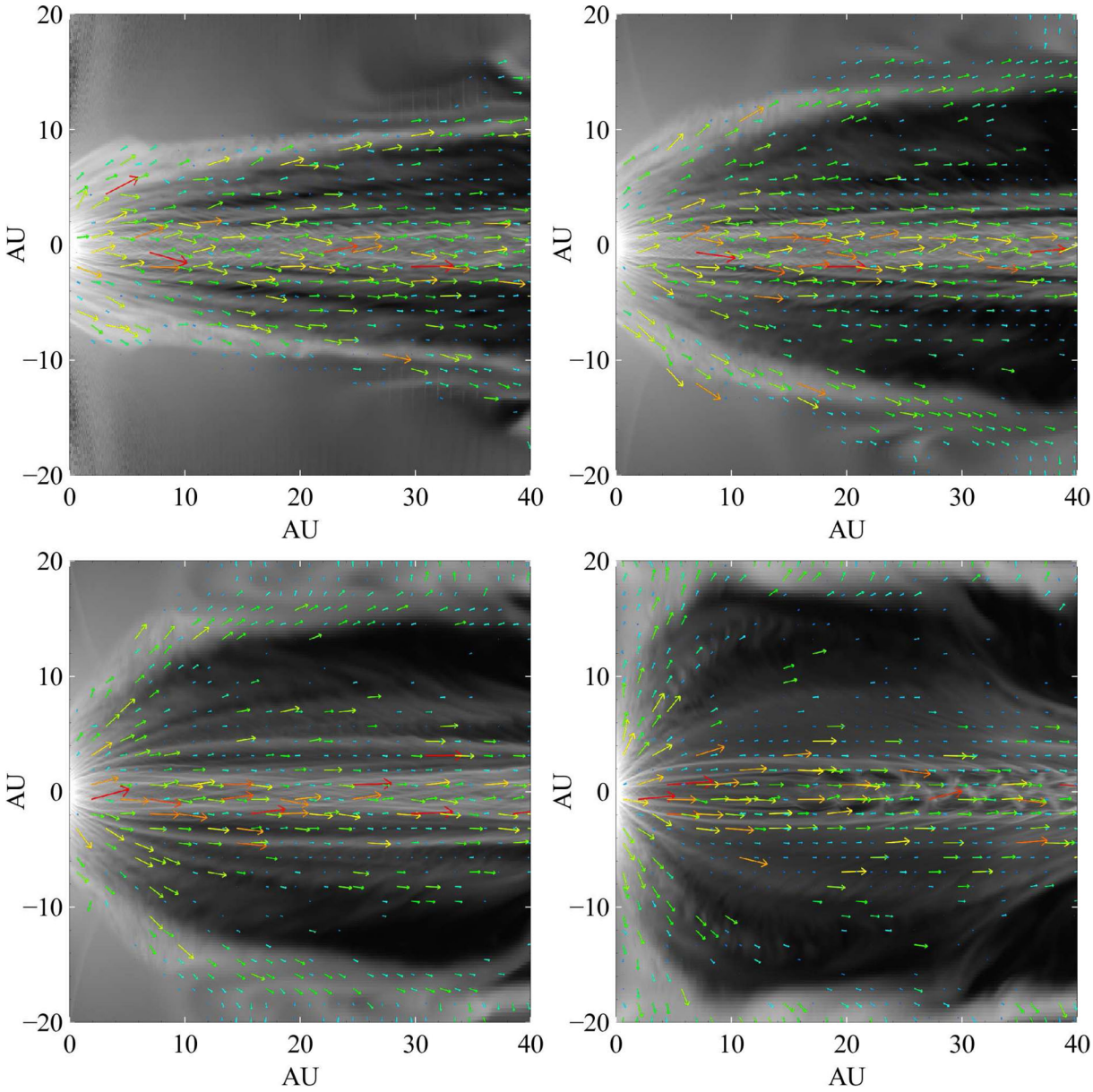

Figure 5. Momentum–density vectors and density shown in a plane along the jet axis. This particular view is focused on a region closer to the disc. The PP jet shows more momentum flowing sideways away from the axis compared to the OP jet in particular. With the weaker magnetic field far from the axis in the PP case, this cannot easily be directed forward, explaining the lack of an outer jet in the PP simulation. Higher momentum vectors are red, lower momentum vectors are blue. The vectors do not have the same normalization for the different simulations.

[S II] line emission maps, that the inner OP jet has an opening angle of about 7°. Again, from the [S II] line emission map (Fig. 7), we find the $\mu = -0.12$ jet to have an opening angle of about 5°.6. The outer jet appears to recollimate (around 35 au for BP, 50 au for $\mu = -0.12$, and around 60 au for the OP jet), but it is unclear if this is due to the interaction with the cocoon. These results agree with Staff et al. (2010), where the BP (more negative μ) jet was found to be narrower than the OP jet.

In Fig. 12 we plot the width of the simulated jets, and compare it with the observed width for DG Tau, UZ Tau, HN Tau, and RW Aur. The width of the simulated jets was found from the [S II] line maps (Fig. 7). As can be seen in Fig. 7, the outer jet in the $\mu = -0.12$ and the BP jets end before the head, making the width decrease for these two jets at 60 au. This is likely an artefact of the jet being so short, had it been much longer, we expect this drop to also occur much farther out, always just behind the head of the jet. It is interesting that the width of the HN Tau jet agrees very well with the OP jet. We also note that the RW Aur jet remains reasonably narrow, making it agree more with the most negative μ simulations (BP and PP).

Hartigan & Morse (2007) found that the HH 30 jet has a constant half-opening angle of 2°.6. We have found that for $\mu > -0.25$, the inner jet opening angle increases with increasing μ. We have also found that the outer jet becomes weaker for more negative μ. Extrapolating our results, we conclude that the HH 30 jet has $-0.25 < \mu < -0.12$, and likely with μ closer to -0.25 than to -0.12. In that case it is likely that the outer jet is very weak, and it may not be observed.

The jets seen in Mg II in Fig. 8 appear quite broken up, with lots of internal structure. These are not related to density fluctuations in the jet, but are rather caused by shocks making parts of the

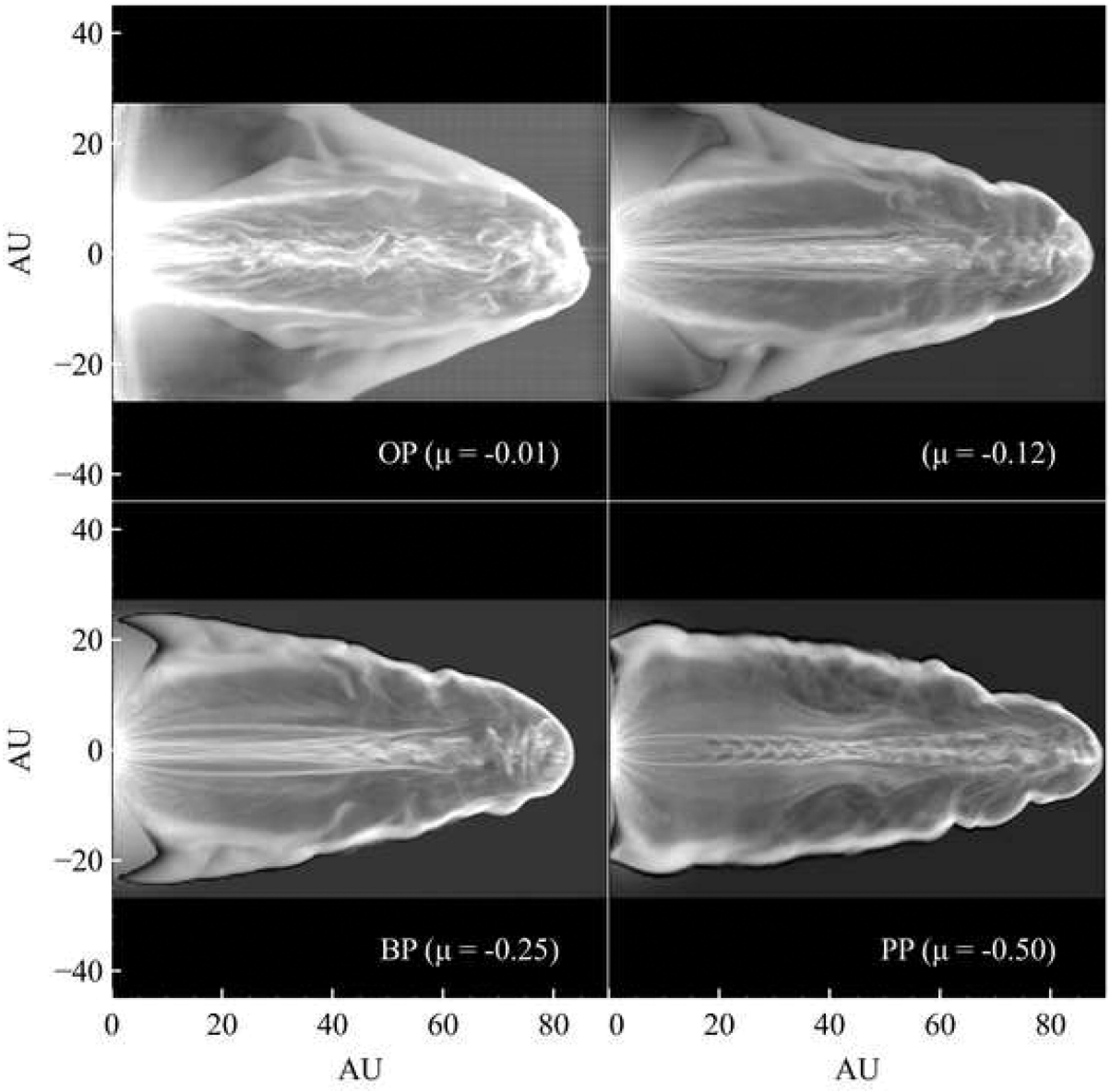

Figure 6. The OP, $\mu = -0.12$, BP, and PP jets seen in [Cl IV] 74 500 Å. The x-axis range is from 0 to 90 au and the y-axis from −45 to +45 au for each image. The disc and the protostar are on the left-hand boundary in these images. See http://quarknova.ucalgary.ca/MHD.html for animation. The normalization factor is different from that in Figs 7 and 8, and the jet would appear much dimmer in this [Cl IV] line than in the [S II] or Mg II line.

jet hotter than other. The jets appear more uniform when seen in S II or Cl IV, this is simply a consequence of how we separate the contours, as explained before. Hartigan & Morse (2007) found knots in the HH 30 jet related to higher excitation but without a density enhancement. These high excitation knots form on a 100 au scale, and could potentially be related to the high excitation knots found in the HH 30 jet.

From the PV diagrams, we see that the maximum velocity perpendicular to the jet axis is around the jet axis (position 0), as can be expected. We find that the largest radial velocities are found in the OP jet with velocities above 100 km s^{-1}, and gradually lower velocities for more negative μ. In the PP jet the maximum perpendicular velocity is found to be about 60 km s^{-1} at 15 au. The maximum velocity found does not differ much between the lines.

4.2 Jet rotation far from the source

In Staff et al. (2010) we found that the Keplerian rotational profile in the disc is inherited by the jet, and is clearly visible in the jet at least 30 au from the disc (the limitations were due to the size of the simulation box). This applied both to the OP and BP jet simulations studied there. For the OP jet, only the inner jet exhibited this feature. We again find the same features in this work. The $\mu = -0.12$ simulation which also has a two-component jet structure also shows the Keplerian-like rotation profile for the inner jet (we have not attempted to fit it with a Keplerian rotation profile). The PP jet, on the other hand, is different in that the kink mode is visible throughout most of the jet (this can be seen as a corkscrew pattern in the PP jet in Figs 6 and 7, and also to some extent in Fig. 8). This kink mode is visible in all the jets closer to the head of the jet (far out). In the PP jet the kink mode does not appear to get out

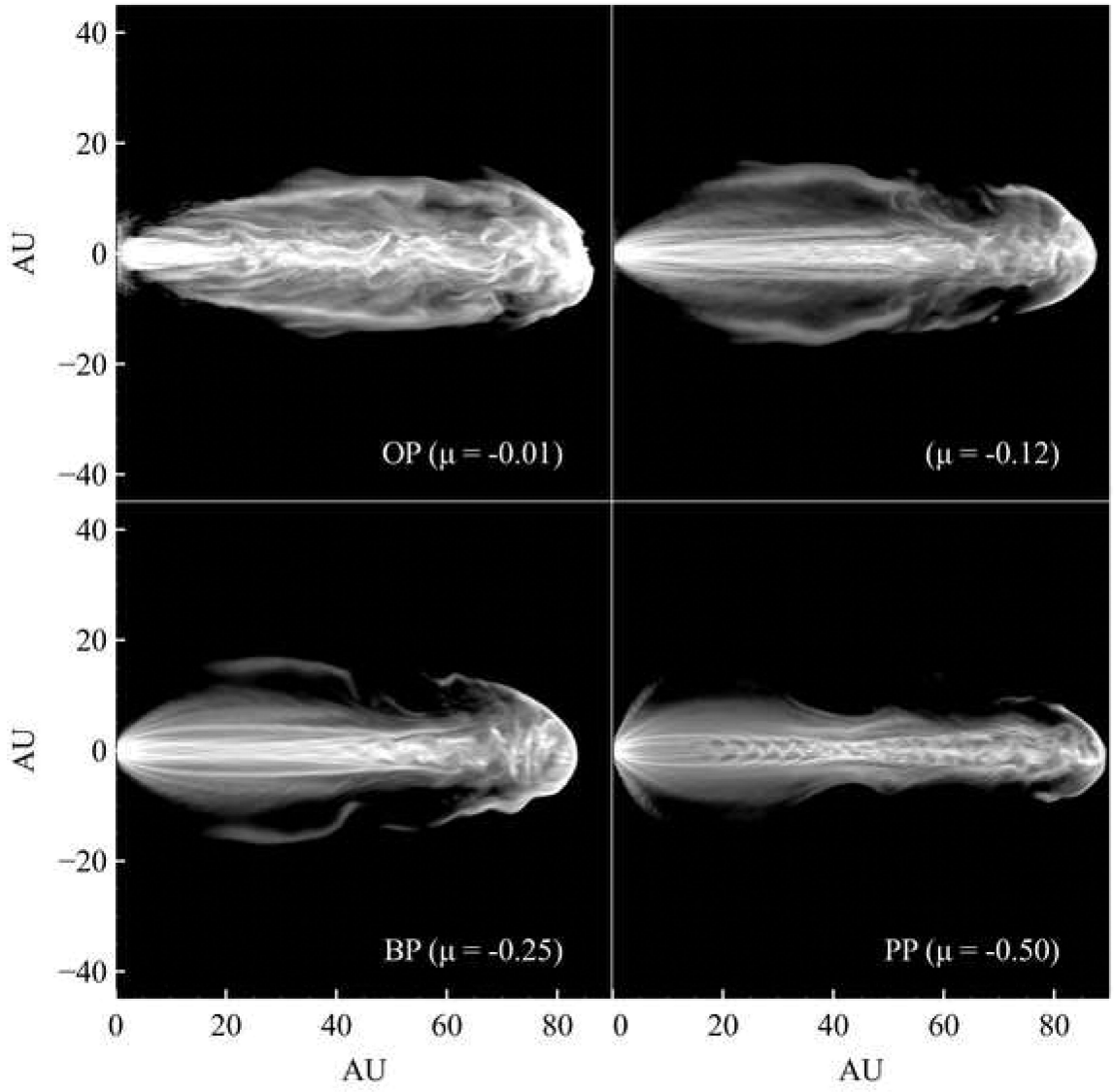

Figure 7. The OP, $\mu = -0.12$, BP, and PP jets seen in [S II] 6730 Å. The x-axis range is from 0 to 90 au and the y-axis from −45 to +45 au for each image. The disc and the protostar are on the left-hand boundary in these images. See http://quarknova.ucalgary.ca/MHD.html for animation. The normalization factor is different from that in Figs 6 and 8, and the jet would appear much brighter in this [S II] line than in the [Cl IV] but much dimmer than in the Mg II line.

of control, while in the other jets the spiral appears to grow farther out in the jet. In the analysis of Pelletier & Pudritz (1992), it was shown that the PP magnetic configuration characterizes a minimum energy state for jets which may explain why this model appears to be more stable than the other three.

Fig. 13 shows a cut perpendicular to the jet axis 24 au from the disc of the density and velocity in the PP jet. At this particular cut it appears as if part of the jet is rotating in one direction, and another part is rotating in the opposite direction. This rotation is also off centred. On this basis, we argue that this is why Coffey et al. (2012) had difficulty finding any indication of rotation in the RW Aur jet.[1]

[1] Animations 'scanning' through the jet, from the disc outwards, for the BP and PP simulations, can be viewed here: http://quarknova.ucalgary.ca/MHD.html The evolution of the density and the magnetic field lines for all the simulations can also be viewed.

In the previous section we showed that the RW Aur jet is rather narrow, and therefore more similar to the more negative μ jets (BP and PP). This is an independent indication that the RW Aur jet may have a steeper power law dependence of the magnetic field (more negative μ) on the disc, that can cause counter rotation and possibly explain the conflicting observations of rotation in this jet.

In the PP configuration with a high magnetic flux close to r_i, matter is very efficiently drained from the region around the axis close to the protostar (within $\sim 1 r_i$). This is the region where no matter is injected from the disc. The resulting extremely low-density region slows down the simulations drastically and we remedy to this by enforcing a floor density which effectively consist of replenishing the region with matter without angular momentum. In all our simulations the gas around the axis near the star is flowing towards the star (backflow), but only in the PP simulation does it change into an outflow. Only a very small region is affected by this, and since we do not draw vectors for all grid cells in Fig. 5, this cannot be seen in that figure.

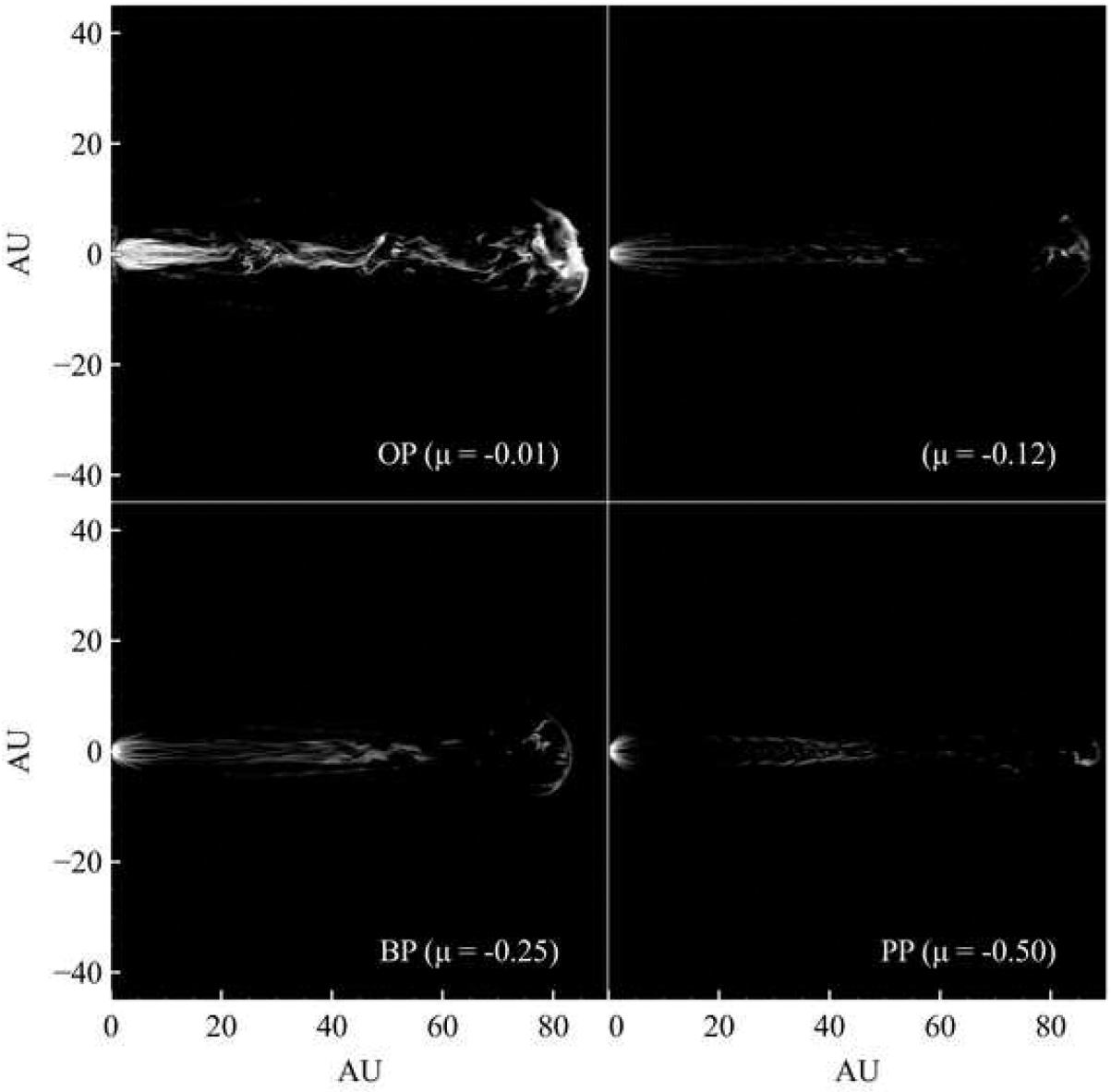

Figure 8. The OP, $\mu = -0.12$, BP, and PP jets seen in Mg II 2796 Å. The x-axis range is from 0 to 90 au and the y-axis from −45 to +45 au for each image. The disc and the protostar are on the left-hand boundary in these images. See http://quarknova.ucalgary.ca/MHD.html for animation. The normalization factor is different from that in Figs 6 and 7, and the jet would appear much brighter in this Mg II line than in the [Cl IV] and [S II] lines.

This low-density outflow is accelerated to large velocity, soon reaching $M_A > 1$. The kink mode instability which can occur when $M_A > 1$ (Díaz et al. 2011) is clearly prominent in the PP case and starts very close to the disc. Furthermore, the strong (i.e. low β) axial magnetic field along the backbone (i.e. in the region within r_i) can sustain and confine a forward non-rotating outflow (in the $+z$-direction). This non-rotating flow is channelled along the backbone and results from the magnetic 'squeezing' of the low-density coronal gas within r_i due to the strong B_ϕ. The $m = -1$ mode grows and is also dynamically important in the PP case in the vicinity of r_i and close to the disc. This complex dynamics leads, in the case of PP, to the rotating and counter-rotating components (and a forward component) as shown in Fig. 14.

The extra mass added on the axis is crucial in order to get counter-rotation, since without it there would not be any matter that could counter-rotate. In reality, this mass could be provided by a wind from the protostar (i.e. Matt & Pudritz 2005). The backflow remains throughout the simulations in all but the PP configuration, and this is why it is difficult to find a counter-rotating component in those configurations. A stellar wind would have to be sufficiently strong to overcome the ram pressure of this backflow in order to get anywhere. That is, only a strong stellar wind could do it. But a strong stellar wind alone will not give counter-rotation. It is also necessary to have twisted field lines along the axis, if not a spiral, being twisted in the direction opposite of the disc rotation that the wind can flow along to cause counter-rotation. However, in order for the gas to follow the field lines rather than just dragging the field with the flow, the magnetic pressure must be greater than the ram pressure of the wind. Hence the wind cannot be too strong.

The gas in the jet that is not part of the spiral continues to rotate clockwise, in the same direction as the disc. In some sense, the PP jet also has two components, though of a very different nature

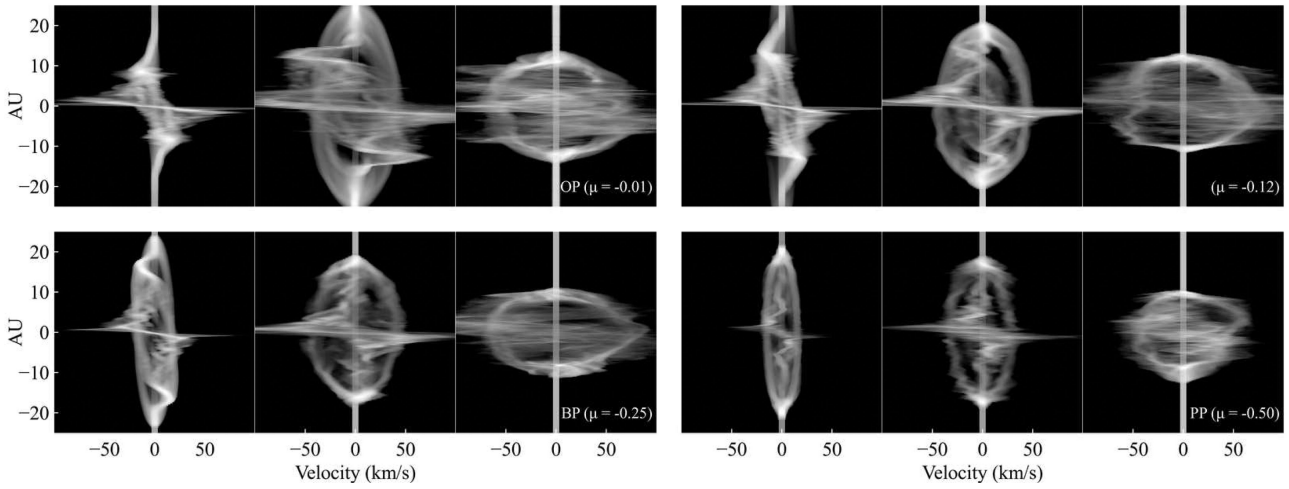

Figure 9. PV diagrams for the OP, $\mu = -0.12$, BP, and PP jets as seen in [Cl IV]. The slit locations are perpendicular to the jet at 15, 45, and 75 au from the disc represented in the left-hand, middle, and right-hand panels, respectively.

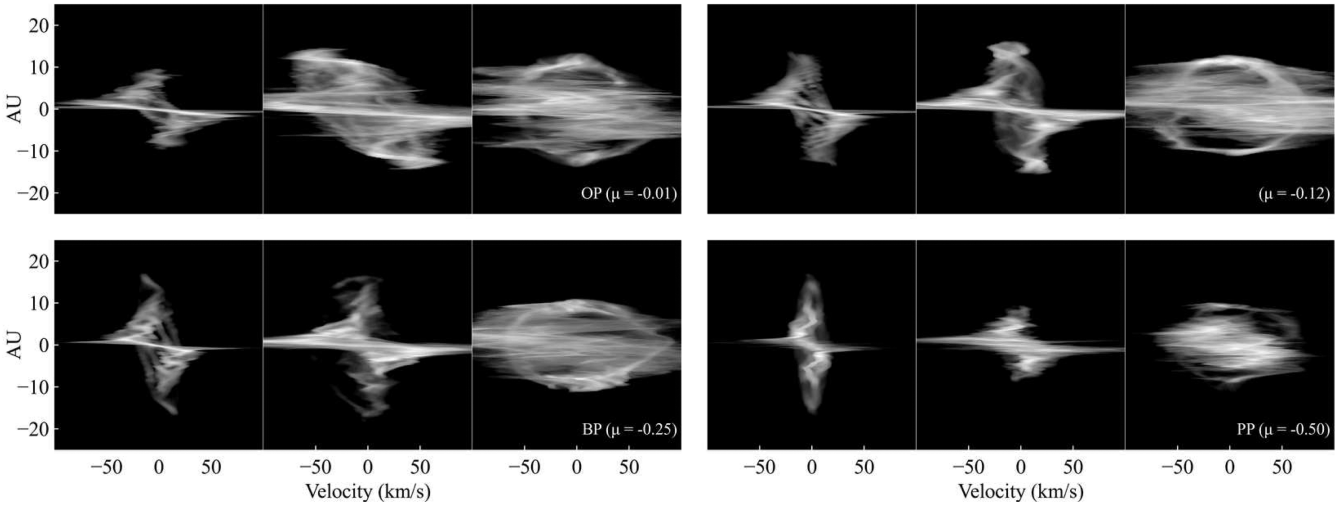

Figure 10. PV diagrams for the OP, $\mu = -0.12$, BP, and PP jets as seen in [S II]. The slit locations are perpendicular to the jet at 15, 45, and 75 au from the disc represented in the left-hand, middle, and right-hand panels, respectively.

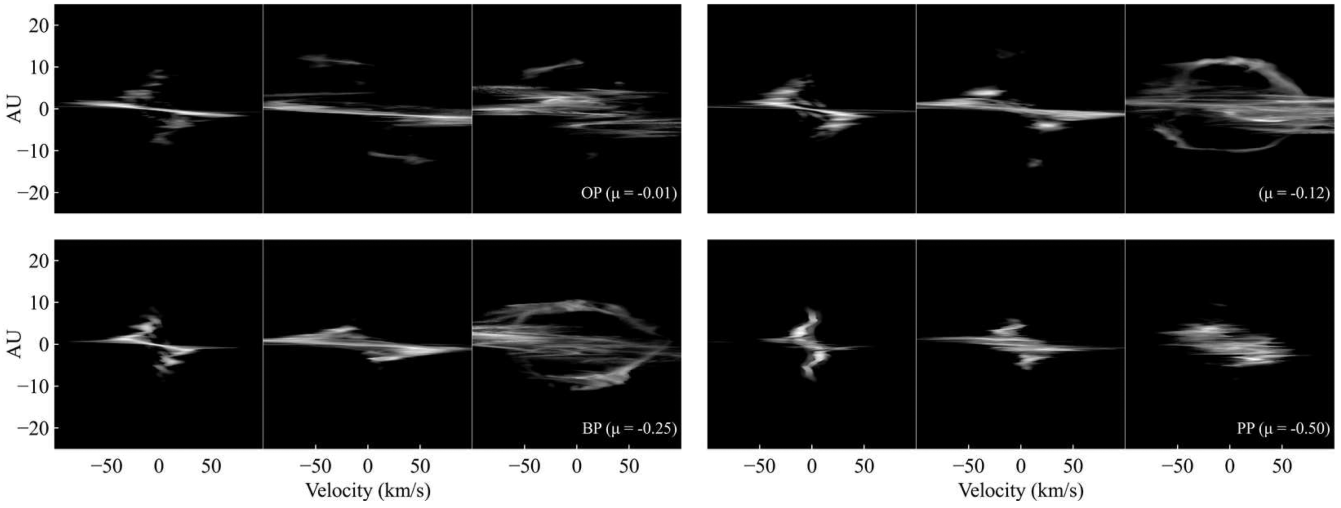

Figure 11. PV diagrams for the OP, $\mu = -0.12$, BP, and PP jets as seen in Mg II. The slit locations are perpendicular to the jet at 15, 45, and 75 au from the disc represented in the left-hand, middle, and right-hand panels, respectively.

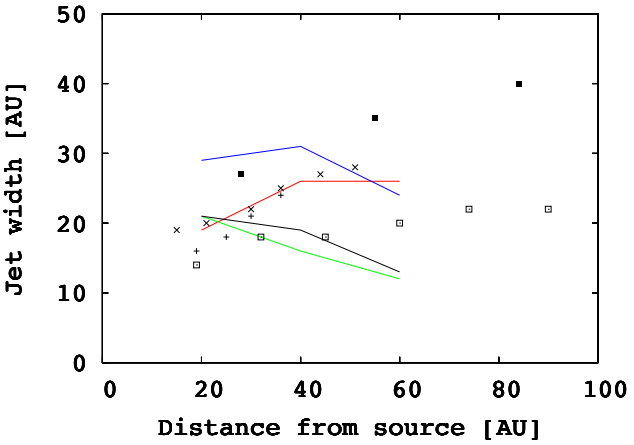

Figure 12. The width of the simulated jets as read off the [S II] figures. Red: OP; blue: $\mu = -0.12$; green: BP; black: PP simulations. The width was measured at 20, 40, and 60 au, and these points simply connected with a line. In addition, we have indicated the width of the DG Tau (filled squares), RW Aur (open squares), UZ Tau (pluses), and HN Tau (crosses), as read off from fig. 2 in Ray et al. (2007).

than the two-component OP and $\mu = -0.12$ jets. In the PP jet, one component counter-rotates, the other corotates with the disc as illustrated in Fig. 14. It is challenging at this stage to assess exactly how much of the jet is counter-rotating. Nevertheless, rough estimate can be derived by looking at Fig. 14. We find that between 10 and 50 au, we observe about 10 per cent counter-rotation. This is not to say that 10 per cent of the mass in the jet is counter-rotating. In fact very little mass is counter-rotating, but it is very hot, making it emits strongly. The likelihood of detecting this depends on how well the jet is observed. The counter-rotating part is reasonably bright, so if more of the fainter gas surrounding the spiral is detected, less counter-rotation should be seen. The counter-rotation becomes less pronounced farther out in the jet, and beyond about 50 au we do not find much counter-rotation. At this point the front of the jet is at 90 au, and we expect that as the jet develops further, the counter-rotating part will also extend further. We note that this is quite different from the counter-rotation found in an analytic study by Sauty et al. (2012).

Whether the observed velocity gradients across the jet are hints of rotation (Pech et al. 2012) or are a result of subjets structure (Soker & Mcley 2012) remains to be confirmed. In general, measuring rotation in jets is a challenging exercise (e.g. Coffey et al. 2012). From the analysis of our simulations we find that many effects can be misinterpreted as rotation. Only by looking at the jet simultaneously in different lines and in PV diagrams can we distinguish clean signs of rotation from velocity gradients induced by MHD modes and those induced by the two-component jets.

4.3 Fluxes and jet energetics

Fig. 15 shows the mass flux, the momentum flux, and the power in the jets. The mass flux for the OP and BP jet can be compared to the mass flux reported in Staff et al. (2010). We now find that both the OP and the BP flux are slightly higher than in Staff et al. (2010), with the difference due to wider jets in the larger simulations. The jet appears to have expanded sideways when propagating from 60 to 90 au. In contrast to Staff et al. (2010), we have simply used a constant jet width along the entire jet, this width is given in Table 1. As in Staff et al. (2010), we find that the mass flux in the OP jet is larger than in the BP jet. The $\mu = -0.12$ jet has an even higher mass flux than the OP jet, only in the very front of the jet has the OP jet higher mass flux indicating that it has piled up more matter in the front. This could in part be because the OP jet has a less pointy front because of the lower Mach number. The mass flux in the PP jet is lower than the mass flux in the BP jet throughout. The observed mass flux in the DG Tau jet (taken from Agra-Amboage et al. 2011) is also shown in Fig. 15. The mass fluxes that we find are comparable to those in observed jets (e.g. Agra-Amboage et al. 2011, for the DG Tau jet). Because the OP jet is faster, the momentum flux in the OP and the $\mu = -0.12$ jets is similar, and the OP jet power is larger.

4.4 Justification of the non-uniform gird: numerical verification

As outlined in Section 2, we use a uniform grid of 100 cells in the x_2 and x_3 directions only between $-25r_i$ and $25r_i$. Beyond this, we use a ratioed grid, in order to stretch the grid size and thereby contain the jet on the grid. Likewise, only 200 cells in the x_1 direction between 0 and $100r_i$ are in a uniform grid, with a ratioed grid beyond that. We have verified that the ratioed grid does not appear to affect the results by making a much smaller grid with $980 \times 660 \times 660$ cells in a uniform grid extending from 0 to $490r_i$ in the x_1 direction, and from $-165r_i$ to $165r_i$ in the x_2 and x_3 directions. In the early phases of the jet evolution, while the jet remains on this smaller grid, we find the same results as on the bigger grid.

In particular, the two-component jet structure in the OP simulation is also apparent at this early phase of the jet evolution. Because of this, we conclude that the existence of a two-component jet structure is not related to the non-uniform grid. At this early stage, the outer jet is also far from any of the boundaries, in particular in the larger simulation box with the ratioed grid, and we conclude that the existence of the outer jet is unrelated to the boundaries of the simulation box.

5 SUMMARY

We have presented the results of four 3D MHD simulations of protostellar jets, with different initial magnetic field structure. The jets are followed (simulated) from the source, and the simulation box stretches out to 90 au along the jet, and 27 au on either side of the jet axis making the simulation box $90 \times 54 \times 54$ au in size.

In order to better compare our results with observations, we have created synthetic emission line maps and PV diagrams. We focused on [S II] 6730 Å and Mg II 2796 Å as these have commonly been used to observe protostellar jets. In addition, we also created synthetic emission line maps in [Cl IV] 74 500 Å which has a much lower critical density than the [S II] and Mg II lines, in order to illustrate the effect of different critical density regimes. We have used these synthetic lines to perform our analysis. The initially more open magnetic field configuration (the PP model), results in the most collimated jet (even when ignoring the possible outer jet in other simulations), with a strong recollimation about halfway through the simulation box. This feature is visible also in the magnetic field lines. The inner jet in the OP and $\mu = -0.12$ simulations appears to have a constant opening angle of about 7°(OP) and 5°.6 ($\mu = -0.12$).

We confirm the results from Staff et al. (2010) regarding jet rotation, that the inner jet in the OP and $\mu = -0.12$ simulations has a Keplerian rotation profile. However, this only extends out a few au from the rotation axis, then the Keplerian rotation profile is broken by the faster rotating outer jet. The BP jet shows a clear Keplerian profile throughout (although there is a slight deviation in

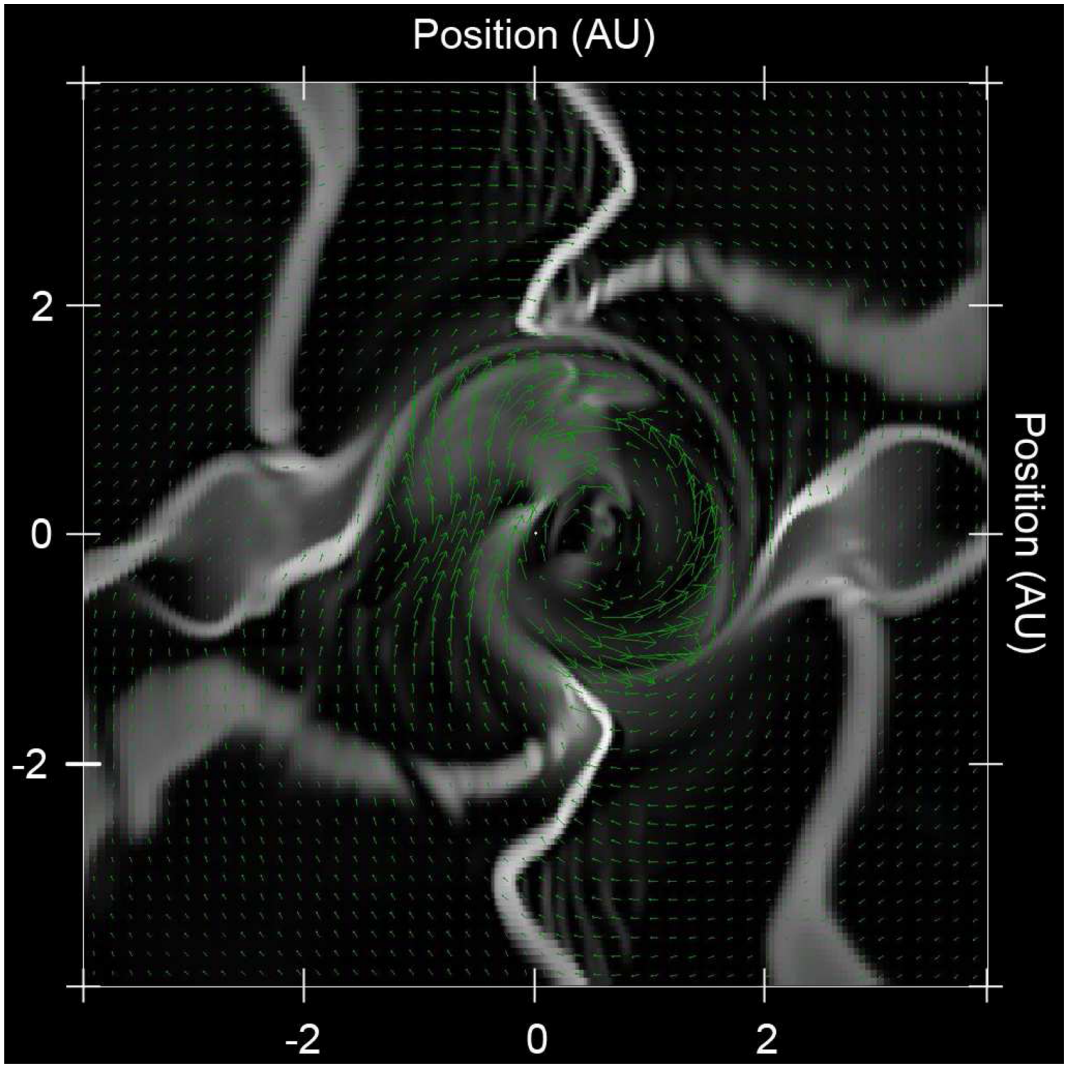

Figure 13. A slice through the PP jet taken perpendicular to the jet 24 au from the disc. Only the innermost ±4 au is plotted for clarity. Shown are filled density contours with the green vectors illustrating the velocity components in that plane. The jet can undergo counter-rotation, and in this particular slice it even appears as if the jet is rotating 'both ways', which is an artefact of the MHD kink ($m = 1$) mode at play.

the rotation profile associated with the weak outer jet). We find that the PP jet is different, in that the kink mode is visible throughout most of the jet. This leads to regions in the jet that are counter-rotating. Hence, memory of the underlying disc Kepler profile is not always preserved. *We emphasize that not observing a Kepler profile does not mean it is not a centrifugal wind.* We also find this corkscrew jet in the outer part of the other simulations, and while the corkscrew feature seems to grow farther from the disc in these simulations, it appears to remain with a constant amplitude in the PP simulation.

Perhaps one of the most important results of our simulations is that it is possible to produce counter-rotating regions in jets as a consequence of kink instabilities. That may explain the observations of counter-rotation in jets such as the RW Aur jet.

Laboratory studies of magnetized plasma jets provide replica of astrophysical jets (e.g. Hsu & Bellan 2002; Ampleford et al. 2008; Frank et al. 2009). In these laboratory jets, the kink mode and spiral-like structure seem to develop in the laboratory jets with similarities with our findings. In Hsu & Bellan (2002), the magnetic field on the 'disc' appears even more open than the PP field which could explain their extreme geometry. However since the 'disc' (the annulus) in these experiments does not effectively rotate the origin of the spiral is harder to understand. In laboratory studies which include rotation (Ampleford et al. 2008) the magnetic field did not play a significant dynamical role unlike what we found in our simulations. Finally, Frank et al. (2009) found that the MHD (kink mode and/or sausage) instabilities in jets break the laboratory plasma jets to into 'chunks' reminiscent of the knotty features we see in the OP jet. The many similarities between laboratory jets and astrophysical jets despite the immense difference in scale speaks to the fundamental nature of the MHD jets.

We still lack a robust explanation for the physics behind the transition from a one- to two-component jet, i.e. how to translate μ into a true physical mechanism that leads to the formation of the outer jet. For now we can only speculate based on a few facts we observed when comparing the launching, formation, and collimation of the jet in the simulations. In the OP and $\mu = -0.12$ simulations, because of the more narrowly opened magnetic field lines along the

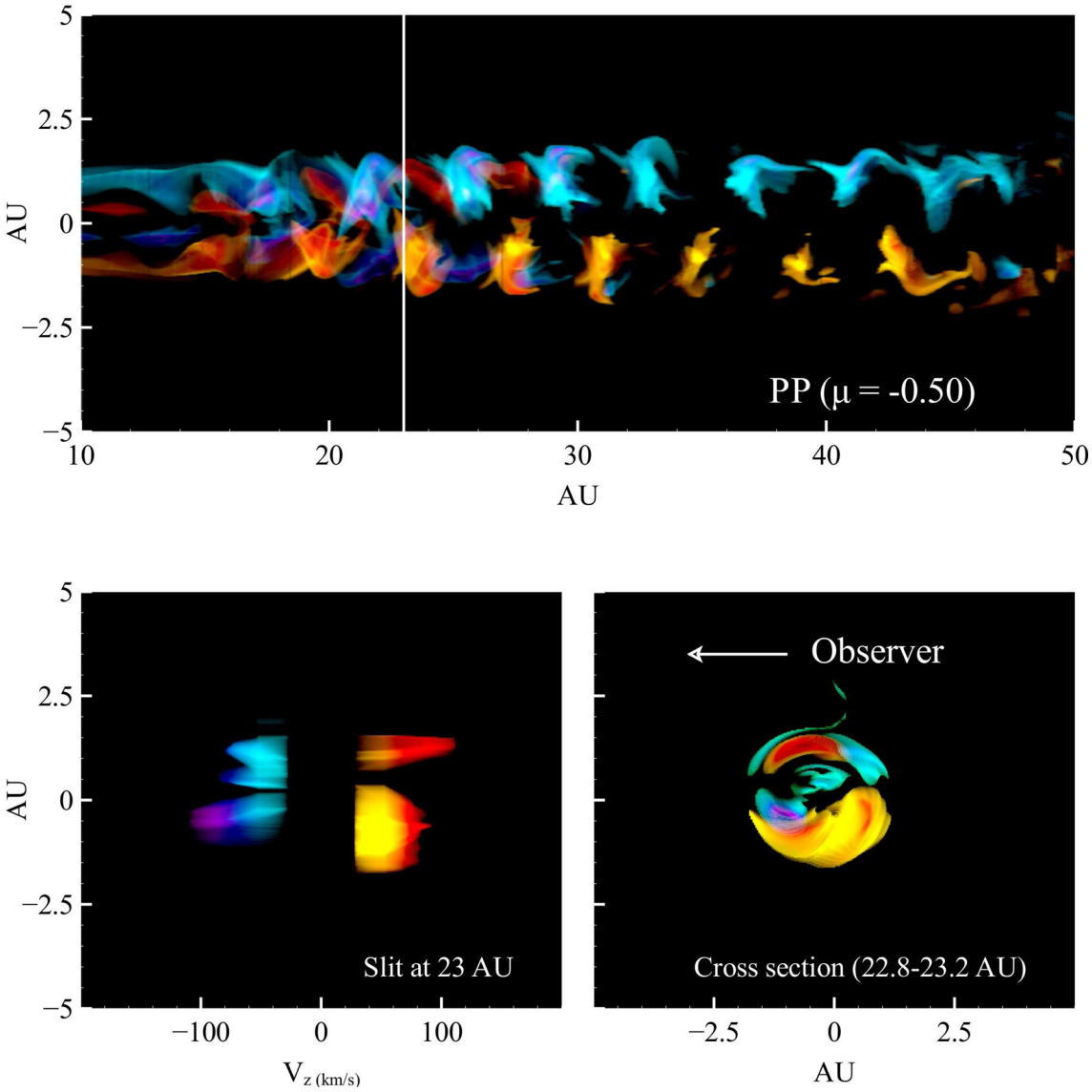

Figure 14. Demonstration of the two rotational components in the PP jet. The top panel shows the rotational velocity of the inner part of the jet. Bluish colours designate gas moving away from us, yellow and reddish colours gas coming towards us. The disc rotates clockwise, i.e. away from us above the axis and towards us below the axis in the top panel. From the very early phases of the jet we see that there is a thin component rotating opposite of the main jet, i.e. towards us (red colour) above the axis, and away from us (blue colour) below the axis. From ∼16 au the spiral occurs, which is this inner component. We make a cut perpendicular to the jet at 23 au (illustrated with a white line), where we make the PV diagram seen in the lower left-hand panel. The lower right-hand panel shows the rotational velocity in this perpendicular slice.

disc, the inner disc region participating in a wind is larger than in the PP and BP cases. Furthermore, the strong backflow seems to split the jet into two components. The PP configuration does not seem to develop a clear outer jet. The material flying out sideways in the PP simulations ends up digging out a bigger cavity around the narrow axial jet. The BP jet appears as an intermediate case, with a very weak outer jet.

There are hints of two-component jets at different scales including AGN (Asada et al. 2010) and maybe in gamma-ray bursts (GRBs; Filgas et al. 2011). This may be an indication, as our simulations suggest, that the μ effect is real and may operate at different scales. This is not an unreasonable assumption given the universal nature of astrophysical jets. We need to perform more simulations by varying μ to assess if there is a critical μ which separates the one-component jets from the two-component jets. If such a critical value exists it is most likely around $\mu = -0.25$. What is evident is the fact that the strength of the outer jet (i.e. for simulations with $\mu \geq 0.25$) increases with μ. For example, we find the outer jet to rotate slower in the $\mu = -0.12$ case than in the OP ($\mu = -0.01$).

These MHD simulations of large-scale disc winds lead to features similar to those of observed low-mass protostellar jets. The jets reach a maximum width of 20–30 au, comparable to the width of observed YSO jets. We find the mass flux in the jet to be of the order $1\text{–}2 \times 10^{-8}\,M_\odot\,yr^{-1}$ (comparable to the observed mass flux in the DG Tau jet), with the more open disc magnetic field configurations (BP and PP) having a somewhat lower mass flux. However, the $\mu = -0.12$ jet has a larger mass flux than the least open disc field configuration (OP), as it is wider. Only in the head of the jet does the

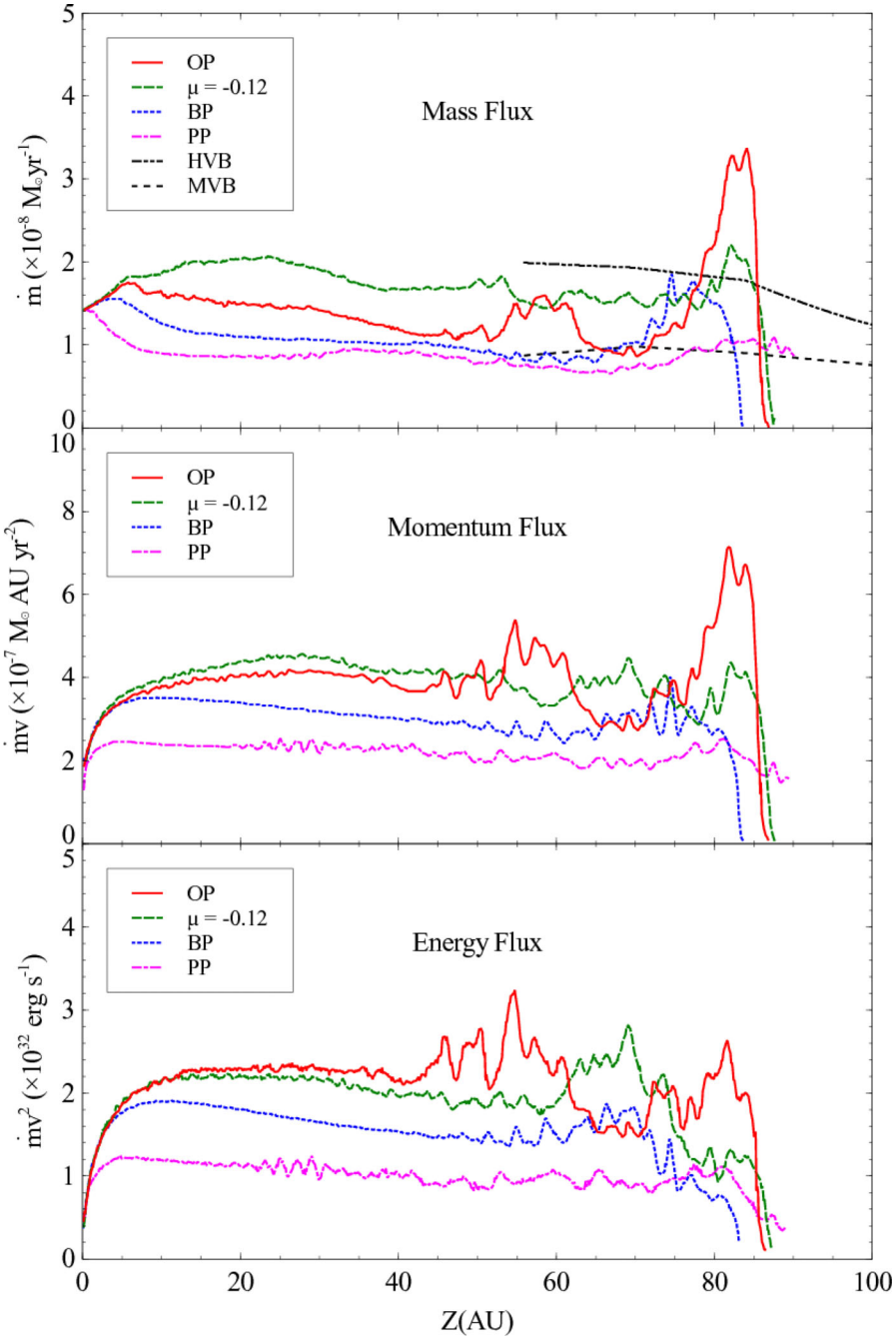

Figure 15. Mass flux (top panel), momentum flux (middle panel), and jet power (bottom panel) along the jet. Red is OP, green is $\mu = -0.12$, blue is BP, and purple is PP. In the mass flux figure, we also overplot the observed mass flux in DG Tau from Agra-Amboage et al. (2011) for the high-velocity blueshifted (HVB) and medium-velocity blueshifted (MVB) intervals. The $\mu = -0.12$ jet has the highest mass flux, but because the OP jet is faster, the two have similar momentum and the OP jet has the higher jet power. The BP and PP jets are generally at lower fluxes throughout the length of the jet.

Table 1. General properties of simulated jets.

	OP ($\mu = -0.01$)	$\mu = -0.12$	BP ($\mu = -0.25$)	PP ($\mu = -0.5$)
Two-components	Yes	Yes	Weak	No
Inner jet opening angle[a]	7.0	5.6	Recollimation[b]	Recollimation[b]
Full width[d]	25 au	30 au	20 au[c]	20 au

[a]The jet opening angle for the OP and the $\mu = -0.12$ jets, which remains fairly constant.
[b]In the BP and PP simulations the jet recollimates and therefore we do not define an opening angle.
[c]Ignoring the weak outer jet.
[d]The maximum jet width for the end state for each magnetic field configuration simulated.

OP jet carry more mass than the $\mu = -0.12$ jet. We have also found that the inner jet preserves the underlying Keplerian rotation profile to large distance. However, for the most open disc magnetic field configuration, the kink mode creates a corkscrew-like jet without a clear Keplerian rotation profile. In this case, we even find regions in the jet rotating opposite to the disc. No outer jet develops in this case. We conclude that magnetized disc winds from underlying Keplerian discs can develop rotation profiles far down the jet that are not Keplerian, or even counter-rotating owing to the operation of kink modes in the jet.

ACKNOWLEDGEMENTS

We thank the anonymous referee for helpful remarks. We thank J. Ge for help with Fig. 1. This work was made possible by the facilities of the Shared Hierarchical Academic Research Computing Network (SHARCNET: www.sharcnet.ca) and Compute/Calcul Canada. JES acknowledges support from the Australian Research Council Discovery Project (DP12013337) program. This work has been supported, in part, by grant AST-0708551 from the US National Science Foundation, and, in part, by grant NNX10AC72G from NASA's ATP program. RO and REP are supported by the Natural Sciences and Engineering Research Council of Canada.

REFERENCES

Agra-Amboage V., Dougados C., Cabrit S., Reunanen J., 2011, A&A, 532, 59
Ampleford D. J. et al., 2008, Phys. Rev. Lett., 100, 035001
Anderson J. M., Li Z.-Y., Krasnopolsky R., Blandford R. D., 2006, ApJ, 653, 33
Asada K., Nakamura M., Inoue M., Kameno S., Nagai H., 2010, ApJ, 720, 41
Bacciotti F., Mundt R., Ray T. P., Eislöffel J., Solf J., Camezind M., 2000, ApJ, 537, L49
Bacciotti F., Ray T., Mundt R., Eislöffel J., Solf J., 2002, ApJ, 576, 222
Blandford R. D., Payne D. R., 1982, MNRAS, 199, 883
Cabrit S., Pety J., Pesenti N., Dougados C., 2006, A&A, 452, 897
Cesaroni R. et al., 2013, A&A, 549, 146
Choi M., Kang M., Tatematsu K., 2011, ApJ, 728, L34
Coffey D., Bacciotti D., Podio L., 2008, ApJ, 689, 1112
Coffey D., Rigliaco E., Bacciotti F., Ray T. P., Eislöffel J., 2012, ApJ, 749, 139
Dere K. P., Landi E., Mason H. E., Monsignori Fossi B. C., Young P. R., 1997, A&AS, 125, 149
Díaz A. J., Oliver R., Ballester J. L., Soler R., 2011, A&A, 533, A95
Ferreira J., 1997, A&A, 319, 340
Filgas R. et al., 2011, A&A, 526, 113
Frank A., Ciardi A., Yirak K., Lebedev S., 2009, Rev. Mex. Astron. Astrofis. (Ser. Conf.), 36, 193
Frank A. et al., 2014, in Beuther H., Klessen R., Dullemond C., Henning Th., eds, Protostars and Planets VI. Univ. Arizona Press, Tucson, in press (arXiv:1402.3553)
Hartigan P., Morse J., 2007, ApJ, 660, 426
Hsu S. C., Bellan P. M., 2002, MNRAS, 334, 257
Jørgensen M., Ouyed R., Christensen M., 2001, A&A, 379, 1170
Kato S. X., Kudoh T., Shibata K., 2002, ApJ, 565, 1035
Krasnopolsky R., Königl A., 2002, ApJ, 580, 987
Krasnopolsky R., Li Z.-Y., Blandford R., 1999, ApJ, 526, 631
Lee C.-F., Ho P. T. P., Bourke T. L., Hirano N., Shang H., Zhang Q., 2008, ApJ, 685, 1026
McKee C. F., Ostriker E. C., 2007, ARA&A, 45, 565
Matt S., Pudritz R. E., 2005, ApJ, 632, L135
Moll R., 2009, A&A, 507, 1203
Murphy G., Ferreira J., Zanni C., 2010, A&A, 512, A82
Norman M. L., 2000, Rev. Mex. Astron. Astrofis. (Ser. Conf.), 9, 66
Osterbrock D. E., Ferland G. J., 2006, Astrophysics of Gaseous Nebulae and Active Galactic Nuclei, 2nd edn. University Science Books, Sausalito, CA
Ouyed R., Pudritz R., 1993, ApJ, 419, 255
Ouyed R., Pudritz R., 1997, ApJ, 482, 712
Ouyed R., Pudritz R. E., 1999, MNRAS, 309, 233
Ouyed R., Pudritz R., Stone J., 1997, Nature, 385, 409
Ouyed R., Clarke D. A., Pudritz R. E., 2003, ApJ, 582, 292
Pech G., Zapata L. A., Loinard L., Rodríguez L. F., 2012, ApJ, 751, 78
Pelletier G., Pudritz R. E., 1992, ApJ, 394, 117
Pudritz R. E., Ouyed R., Fendt Ch ., Brandenburg A., 2007, in Reipurth B., Jewitt D., Keil K., eds, Protostars and Planets V. Univ. Arizona Press, Tucson, p. 277
Ramsey J. P., Clarke D. A., 2011, ApJ, 728, L11
Ray T., Dougados C., Bacciotti F., Eislöffel J., Chrysostomou A., 2007, in Reipurth B., Jewitt D., Keil K., eds, Protostars and Planets V. Univ. Arizona Press, Tucson, p. 231
Sauty C., Cayatte V., Lima J. J. G., Matsakos T., Tsinganos K., 2012, ApJ, 759, L1
Sheikhnezami S., Fendt C., Porth O., Vaidya B., Ghanbari J., 2012, ApJ, 757, 65
Shibata K., Uchida Y., 1985, PASJ, 37, 31
Shu F., Najita J., Shang H., Li Z.-Y., 2000, in Mannings V., Boss A. P., Russell S. S., eds, Protostars and Planets IV. Univ. Arizona Press, Tucson, p. 789
Soker N., Mcley L., 2012, preprint (arXiv:1209.0986)
Staff J. E., Niebergal B. P., Ouyed R., Pudritz R. E., Cai K., 2010, ApJ, 722, 1325
Staff J. E., Koning N., Ouyed R., Pudritz R., 2013, in Gómez J. L., ed., EPJ Web of Conferences, Vol. 61, The Innermost Regions of Relativistic Jets and Their Magnetic Fields. EDP Sciences, France, p. 02006 (published online)
Steffen W., Koning N., Wenger S., Morisset C., Magnor M., 2011, IEEE Trans. Visualization Comput. Graphics, 17, 454
Uchida Y., Shibata K., 1985, PASJ, 37, 515
Ustyugova G. V., Koldoba A. V., Romanova M. M., Chechetkin V. M., Lovelace R. V. E., 1995, ApJ, 439, L39
Vural J. et al., 2012, A&A, 543, A162
Woitas J., Bacciotti F., Ray T. P., Marconi A., Coffey D., Eislöffel J., 2005, A&A, 432, 149
Zanni C., Ferrari A., Rosner R., Bodo G., Massaglia S., 2007, A&A, 469, 811
Zhang Y. et al., 2013, ApJ, 767, 58

This paper has been typeset from a TEX/LATEX file prepared by the author.